Linear control of thermoacoustic oscillations with flame dynamics modeled by a level-set method

Xiaoling Chen[a], Santosh Hemchandra[b], Hosam Fathy[c], Jacqueline O'Connor[a,*]

[a] *The Pennsylvania State University, University Park, PA 16802, USA*
[b] *Indian Institute of Science, Bengaluru, KA 560012, India*
[c] *University of Maryland, College Park, MD 20742, USA*

Abstract

This article focuses on co-simulation of the coupled nonlinear dynamics of flame heat release rate, acoustics, and feedback control in an active thermoacoustic oscillation control system. This work is motivated by an extensive existing body of literature showing the potential of closed-loop active control to suppress thermoacoustic oscillation. Linear algorithms such as linear quadratic Gaussian (LQG) control are often used for thermoacoustic oscillation control, with the important caveat that flame heat release rate oscillation is often highly nonlinear. This creates a need for a tool that can co-simulate the coupled nonlinear thermoacoustic dynamics with linear control. The main contribution of this article is the development of a tool capable of co-simulating nonlinear heat release dynamics using a level-set formulation, together with linear acoustics plus a linear feedback controller. The article demonstrates this framework on an LQG-controlled wedge flame in a unidimensional Rijke tube. The nonlinear thermoacoustic model is formed in a modified level-set solver by connecting the linear acoustics to the original nonlinear flame dynamics via a velocity convection equation. This framework succeeds in preserving the nonlinearity of the thermoacoustics in the Rijke tube without the LQG control. For the flame-driven Rijke tube in this article, LQG control is successful in suppressing the nonlinear thermoacoustic oscillation. In addition, the simulation based on the

---

[*] Corresponding author
Email address: `jxo22@psu.edu` (Jacqueline O'Connor)

framework is useful in elucidating the impact of factors such as flame location, flame temperature rise, and the timing of the onset of LQG control on the instability suppression performance and energy needs.

Keywords:
Thermoacoustic oscillation, level-set flame dynamics, active control

---

1. Introduction

Modern gas turbine combustors apply lean-premixed combustion to satisfy the low $\mathrm{NO_x}$ emission requirement in the power industry. Thermoacoustic oscillation is an undesirable issue in lean-premixed combustion systems [1] and manifests as large amplitude pressure oscillations. It is generated by the feedback coupling between flame heat release rate oscillations and combustor acoustic perturbations [2], where the flame heat release rate oscillation serves as an energy source for the acoustics. The acoustics inside the combustor affect the flame heat release rate and this relation is captured by a flame describing function (FDF) [3, 4, 5]. To attenuate or even avoid thermoacoustic oscillations, active control has been extensively studied in the literature and demonstrated to be effective, especially model-based control [6, 7].

Among different methods used for model-based control design, physics-based modeling of the thermoacoustic system captures more knowledge compared to empirical modeling and is more effective in suppressing the thermoacoustic oscillations in practical systems. A physics-based model of a thermoacoustic system is built by connecting the heat release dynamics model to an acoustic solver. In gas turbine combustors, acoustics are assumed to be linear since the pressure oscillation amplitude is usually two orders of magnitude smaller than the mean pressure. The heat release rate dynamics can be either linear or nonlinear depending on the oscillation amplitude and frequency. When the oscillation amplitude is small, a linear time-lag model $(n-\tau)$ can be used to describe the flame dynamics [8]. In this situation, the flame heat release rate is proportional to the velocity oscillation with a time delay; this flame model has been useful in analyzing the instability of certain thermoacoustic systems [9, 10]. For most practical flames, the flame dynamics are nonlinear and usually modeled by a flame describing function (FDF). The FDF captures the nonlinear dependence of flame heat release oscillations on the acoustic perturbations upstream of the flame [3]. This dependence has been observed in some experimental studies [11, 3, 12]. The nonlinear flame dynamics features are included in prediction of limit cycle amplitudes [3, 5, 13, 14], and can explain mode switching and instability triggering behaviors [3, 15, 16, 17], including spinning modes in annular combustors [18]. Compared to the linear $n-\tau$ model, the FDF is more accurate in capturing the flame dynamics and describing the nonlinear dynamics in the thermoacoustic system. A control design based on an FDF will likely perform better at suppressing oscillations.

In describing the flame dynamics, the level-set formulation, sometimes referred to as a “G-equation” formulation, is one of the methods that captures the nonlinearity in flame heat release response [19, 20, 21, 22, 23]. Initially used by Fleifil et al. [21] to model heat release rate dynamics in the presence of acoustic fluctuations, the method captures one of the key sources of nonlinearity in flame dynamics: kinematic restoration [24]. Previous studies have considered the nonlinear dynamics of Rijke tubes using level-set models to study the nonlinear behaviors of thermoacoustic systems [25, 26, 15, 16, 17]. Dowling [25] derived a kinematic model of the response of the flame to flow disturbances from a more general G-equation and coupled this kinematic flame model with the acoustic waves generated in the duct. The nonlinearity is observed in the system from the time evolution of disturbances. Kashinath et al. [26] modeled the flame using a nonlinear kinematic model based on the G-equation. The time-domain simulation of the coupled thermoacoustic system is performed with a Galerkin discretization for acoustic pressure and velocity. The heat release rate in the time-domain simulation is highly nonlinear and the limit cycle predictions agree with the frequency domain analysis. Kashinath et al. [15] furthered the nonlinear analysis in a similar system. The study focused on a two-dimensional premixed Bunsen flame numerically simulated by a G-equation coupled with duct acoustics and examined the bifurcations and routes to chaos for three control parameters. Waugh et al. [16] considered a ducted axisymmetric premixed flame using a level-set solver. They improved the calculation efficiency of the bifurcations from the limit cycles using matrix-free continuation methods. Orchini et al. [17] coupled a level-set kinematic model for a laminar flame with a state-space realization of the linearized acoustic equations to form a low-order time-domain model. They investigated the nonlinear stability of the thermoacoustic system, both in the frequency and time domains. These studies show the potential of applying the similar method for control applied closed-loop thermoacoustic system.

Thermoacoustic oscillation can be attenuated using either linear or nonlinear control algorithms, with the former being more common. There have been several studies of applying linear control to suppress nonlinear thermoacoustic oscillations. Different controls are selected for thermoacoustic oscillations with different levels of nonlinearity in the instability model [27, 28, 29, 30]. Though some researchers initially treat the nonlinearity in a manner similar to model uncertainty, then evaluate the stability of the closed loop system with a controller using the integral quadratic constraints method [29]. The most often used control for nonlinear thermoacoustic oscillations is linear quadratic Gaussian (LQG) control [31, 32, 33]. LQG control is composed of two parts: a linear quadratic regulator (LQR) and a Kalman filter [34]. The idea behind LQR is to design a stabilizing control input for a linear system that simultaneously optimizes a quadratic cost function in the system states and control inputs [35]. The Kalman filter, which can be regarded as a noise attenuator, estimates the system states from observed noisy measurements [34]. Compared to phase-shift control [36], the main advantage of LQG control is that it can suppress multiple instability modes instead of single mode. LQG has been successfully applied to suppress thermoacoustic oscillation in some laboratory combustors [31, 32, 37, 38].

The literature shows that it is promising to apply linear control to suppress nonlinear thermoacoustic oscillations, and so the goal of this work is to explore the utility of linear control on nonlinear thermoacoustic oscillations. In this work, we adopt a level-set solver to describe the nonlinear flame dynamics and model the thermoacoustic system with LQG control. The thermoacoustic model, describing the thermoacoustic oscillations in a unidimensional Rijke tube, is formed by adding a linear state-space acoustic model to a level-set solver, which describes the nonlinear flame dynamics. The LQG controller is designed based on a linearization of the flame describing function of this flame. We then apply the LQG controller to the original thermoacoustic model, which is realized by connecting the LQG controller with the level-set solver. There are certain limitations to using a level-set formulation for modeling flame dynamics. In particular, the formulation does not conserve momentum or energy across the flame; the implications of this will be noted in the results of our work. However, the level-set formulation provides two major advantages over other flame modeling strategies. First, it faithfully captures the nonlinear behavior of flames that arises from kinematic restoration, which a model like $n - \tau$ would not. Second, it is computationally efficient, and provides the required nonlinearity at relatively little cost as compared to other options like computational fluid dynamics. Given the successes of previous studies using this method as well as these two benefits, it's an appropriate framework for exploring the central question of this work, which focuses on the application of linear control to nonlinear flame dynamics.

In this work, we choose to use a wedge flame, rather than the previously-used Bunsen flame approach, for three reasons. First, previous work has explored the system dynamics of Rijke tubes driven by Bunsen flames [21, 39, 40, 41, 42, 15]. Second, wedge flames can display higher levels of nonlinearity in the flame response because only the base of the flame is bounded, whereas Bunsen flames are bounded by both the stabilization boundary condition and the "closed tip" boundary condition at the top [43, 44, 45, 46, 47, 48]. To test the limits of control in the context of nonlinear behavior, the wedge flame provides more of a challenge. Finally, flames in realistic devices like gas turbines tend to resemble confined wedge flames, although the stabilization mechanism often involves swirl, not just a bluff body [49, 12, 50, 51, 52, 53, 4]. Despite this, this flame description moves one step closer to understanding the opportunities for active control of thermoacoustic oscillations by incorporating more realistic flame geometries and models.

2. Methods

2.1. Flame-driven Rijke Tube

The Rijke tube configuration considered in this work is based on an experiment designed for a previous study of thermoacoustic model identification [54], which is similar to other flame-driven Rijke tube experiments [41]. The Rijke tube's cross-sectional view is shown in Fig. 1. It has a length of L and a radius of r_o. Air flows into the outer tube at a velocity of u_{bulk}. The flame is stabilized on an inner tube with radius r_i, where a reactant mixture of methane and air with an equivalence ratio ϕ flows into the inner tube at velocity of u_0. An acoustically-compact, confined wedge flame is stabilized at the flame location b_f. We assume an isentropic, homogeneous, and steady mean flow as well as a step temperature rise across the flame in the Rijke tube. The temperatures of both the reactants in the inner tube and the air in the outer tube are T_1 and the temperature downstream of the flame is assumed to be a constant T_2.

Given the aspect ratio of the Rijke tube, we only consider longitudinal acoustics in the axial coordinate x and neglect transverse modes. The acoustic characteristics of the flame-driven Rijke tube are largely dependent on the flame location b_f and temperature distribution along the Rijke tube $T(x)$. Following the work of Dowling and Stow [55], we obtain the linearized momentum and energy conservation equations for the Rijke tube in Eq. (1) and Eq. (2). These equations assume that: (i) the mean flow occurs at a small Mach number (*i.e.*, the bulk flow velocity u_{bulk} is low); (ii) fluctuations in density, pressure, velocity, and temperature around equilibrium states are small; (iii) the acoustic damping is neglected. The work presented in this paper is based on a Rijke tube model

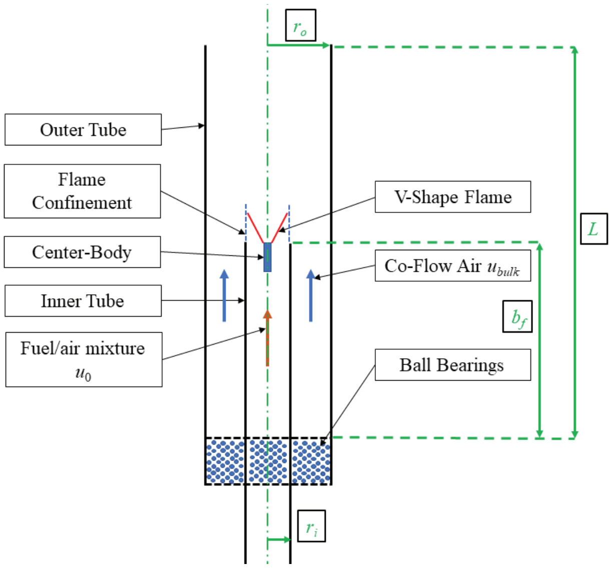

FIGURE 1. Rijke tube cross-section schematic

with assumptions made above.

$$\bar{\rho}\frac{\partial u'}{\partial t} = -\frac{\partial p'}{\partial x} \tag{1}$$

$$\frac{\partial p'}{\partial t} = -\bar{\rho}\bar{c}^2\frac{\partial u'}{\partial x} + (\gamma - 1)q' \tag{2}$$

In this model, $\bar{\rho}$ and $\bar{c}$ are mean density and mean speed of sound. The variables u', p', and q' represent the fluctuating velocity, pressure, and heat release rate per unit volume from the flame, respectively. The independent variables are time t and axial direction x. The constant γ is the ratio of specific heats. Based on the acoustic compactness of the flame, the fluctuating heat release rate per unit volume is described by a product between the heat release rate per unit cross-sectional area of the Rijke tube Q' and a Dirac delta function, as shown in Eq. (3).

$$q'(x,t) = Q'(t)\delta(x - b) \tag{3}$$

The inlet is assumed to be an acoustically closed boundary, where the acoustic velocity fluctuation is zero. The exit of the Rijke tube is open to the atmosphere and regarded as an acoustically open boundary, where the pressure fluctuation is zero. The two boundary conditions are close to those of the actual combustor and they are summarized in Eq. (4). However, there are limitations of the application of a Rijke tube to study thermoacoustic oscillations in actual gas turbine combustors. The application of the Rijke tube in this study serves the goal of understanding the application of linear control to nonlinear thermoacoustic oscillations. Compared to real gas turbine combustors, the Rijke tube has following limitations: (i) the radius of a Rijke tube is constant while there is a sudden area expansion near the dump plane in a gas turbine combustor; (ii) flow velocity and pressure is very low in a Rijke tube compared to those in an actual combustor; (iii) only longitudinal acoustic mode is considered in a Rijke tube while transverse acoustic mode exists in some gas turbine combustors; (iv) the flame is assumed to be a compact heat release source in a Rijke tube, whereas this may not be the case in all combustor configurations.

$$u'(x=0,t)=0,\ p'(x=L,t)=0 \tag{4}$$

2.2. Acoustic Model

Due to the the step increase of the mean temperature across the flame, there is a discontinuity of mean speed of sound $\bar{c}(x)$ and mean density $\bar{\rho}(x)$ at the flame location. Similar to the wave-based method by Dowling [56], we consider the two regions upstream and downstream of the flame separately, as shown in Eq. (5) and Eq. (6). In each region, the mean variables $\bar{c}(x)$ and $\bar{\rho}(x)$ are constant and the flame location is the boundary between regions. The location just upstream of the flame boundary is b^- and the location just downstream of the flame boundary is b^+. At the boundary, two conditions are enforced, as shown in Eq. (7). First, pressure must be continuous, such that the pressure fluctuation is equal on either side of the flame location. Second, the difference of velocity oscillation across the flame is caused by the heat release rate oscillation per unit area $Q'(t)$.

$$\bar{\rho}_1 \frac{\partial u'}{\partial t} = -\frac{\partial p'}{\partial x}, \ \frac{\partial p'}{\partial t} = -\bar{\rho}_1 \bar{c}_1^2 \frac{\partial u'}{\partial x} \tag{5}$$

$$\bar{\rho}_2 \frac{\partial u'}{\partial t} = -\frac{\partial p'}{\partial x}, \ \frac{\partial p'}{\partial t} = -\bar{\rho}_2 \bar{c}_2^2 \frac{\partial u'}{\partial x} \tag{6}$$

$$\begin{aligned} p'(x = b^-, t) &= p'(x = b^+, t) \\ u'(x = b^+, t) - u'(x = b^-, t) &= \frac{\gamma - 1}{\bar{\rho}\bar{c}^2} Q'(t) \end{aligned} \tag{7}$$

The original acoustic model is infinite-dimensional. In a practical combustor, high-frequency modes are damped and the dominant acoustic modes are on the order of hundreds of Hertz. The combustor can sustain multiple modes, however, and the acoustic pressure or velocity inside the system can be written as a superposition of the multiple modes. For these reasons, we apply an expansion to represent the acoustic variables u' and p' as products of time-dependent coefficients and spatial orthogonal basis functions. We then use Galerkin projection to substitute the expanded acoustic variables into the original partial differential equations, multiply the equations with a basis function, and integrate over the spatial domain. This method converts the original partial differential equations to a set of ordinary differential equations describing the dynamics of the time-dependent coefficients; details of this process are described in the supplemental material. In the expansion, we select shifted Legendre polynomials as the basis functions. The original Legendre polynomials are defined in region $[-1, 1]$. To make the basis functions orthonormal within the region $[0, 1]$, which is the spatial domain for the normalized governing equations, we shift the original Legendre polynomials to region $[0, 1]$ with appropriate scale factors. The detailed process of obtaining the shifted Legendre polynomials are described in the supplemental material.

The set of ordinary differential equations after Galerkin projection serves as the state space form of the acoustic model, whose state variables are the time-dependent coefficients in the expansions of velocity u' and pressure p'. The magnitudes of the two acoustic variables usually differ by at least two to three orders of magnitude, which would make the state matrix of the state space model numerically ill-conditioned. To ensure a well-conditioned state matrix, the two acoustics variables and the heat release rate oscillations are normalized by the following reference values: u_0, p_{atm}, and Q_0.

Both the mean mixture flow velocity, u_0, and heat release rate per unit area, Q_0, are linked to the shape of the wedge flame. In this paper, the steady wedge flame is stabilized on a center-body with negligible width compared to the inner tube radius r_i, as shown in Fig. 2. For an equivalence ratio ϕ, the laminar flame speed S_L is calculated using the GRI-3.0 mechanism, as in Ref. [57]. The steady wedge flame shape (blue line) is determined by the relation between the flame speed S_L and incoming mixture flow velocity u_0, as in Eq. (8), where the flame aspect ratio β is the ratio between the flame length L_f and flame width/radius R_f. In addition to the flame speed, the mixture density ρ_m and heat of combustion per unit mass of the mixture $h_{R,m}$ also depend on the equivalence ratio. Knowing the above variables of the mixture and the outer tube radius r_o, we can determine the mean heat release rate of the flame per unit cross-sectional area of the outer tube Q_0, as indicated in Eq. (8). The detailed formula to determine the mean mixture flow speed and heat release rate per unit area is in Eq. (8), where subscript "m" represents the mixture.

$$
\begin{aligned}
u_0 &= S_L\sqrt{1+\beta^2} \\
Q_0 &= \frac{\rho_m(\phi)S_L(\phi)h_{R,m}(\phi)A_{f,0}}{\pi r_o^2} \\
A_{f,0} &= \pi r_i^2\sqrt{1+\beta^2}
\end{aligned}
\tag{8}
$$

Knowing the mean variables for velocity, heat release rate per unit area and flame area, the governing partial differential equations for the normalized acoustic variables are in Eq. (9) and Eq. (10). When considering control applications, the actuator is selected to be a speaker mounted at the Rijke tube inlet, providing the acoustic velocity signal $u_{n,c}$ as the control input to attenuate

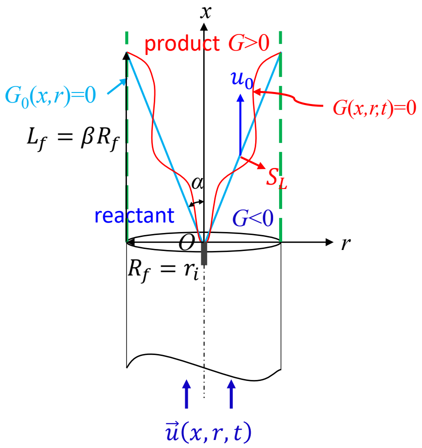

FIGURE 2. Wedge flame stabilized on a center-body described by a level-set method

the pressure oscillations. This leads to the updated boundary conditions in Eq. (11).

$$\frac{\partial u_n'}{\partial t} = -\frac{p_{atm}}{\bar{\rho} u_0}\frac{\partial p_n'}{\partial x} \tag{9}$$

$$\frac{\partial p_n'}{\partial t} = -\frac{\bar{\rho}\bar{c}^2 u_0}{p_{atm}}\frac{\partial u_n'}{\partial x} + (\gamma - 1)\frac{Q_0}{p_{atm}}\delta(x-b)Q_n' \tag{10}$$

$$u_n'(x=0,t) = u_{n,c}(t),\ p_n'(x=L,t) = 0 \tag{11}$$

The order of the state space model depends on the number of expansion terms used to approximate the acoustic variables. Based on the system characteristics, we apply model order reduction to focus on the dynamics of a finite number of the coefficients, which correspond to a finite number of modes. Similar to the balanced truncation method applied by the authors in earlier work [58], we truncate the system to an order of 8 to capture the first four acoustic modes. The two inputs of the model are the normalized oscillating heat release rate per unit area Q_n' and velocity from the actuator at the Rijke tube inlet $u_{n,c}'$, in the cases when a controller is applied. This velocity is zero when the controller is not activated. The two outputs of the model are the normalized oscillating velocity just upstream of the flame $u'_{n,b}$ and the pressure at the Rijke tube inlet $p'_{n,0}$. The state space form of the acoustic model is in Eq. (12).

$$\dot{\boldsymbol{x}} = A_n \boldsymbol{x} + B_n \begin{bmatrix} Q'_n \\ u_{n,c} \end{bmatrix}, \quad \begin{bmatrix} u'_{n,b} \\ p'_{n,0} \end{bmatrix} = C_n \boldsymbol{x} + D_n \begin{bmatrix} Q'_n \\ u_{n,c} \end{bmatrix} \tag{12}$$

2.3. Flame Dynamics

The flame dynamics are described by a level-set G-equation model examined in earlier work by one of the authors [57]. The model assumes that the G-field is a smooth scalar field and the flame is tracked by the iso-contour $G{=}0$; this surface separates the reactants ($G{<}0$) from the products ($G{>}0$), as shown in Fig. 2. The instantaneous flame position, which is denoted by the scalar field G, is governed by the G-equation in Eq. (13).

$$\frac{\partial G}{\partial t} + \vec{u} \cdot \vec{\nabla} G = S_L |\vec{\nabla} G| \tag{13}$$

where $\vec{u}$ is the local flow velocity vector, and S_L is the laminar flame speed. In addition to the steady flame location described by the level-set $G_0 = 0$, Figure 2 also illustrates the instantaneous wedge flame $G(x, r, t)$ (red curve) with oscillating incoming flow velocity $\vec{u}(x, r, t)$. The fluctuating flame position causes the fluctuating flame area A_f, which is calculated using the integral equation in Eq. (14). Assuming constant mixture density ρ, heat of combustion per unit mass of the mixture h_R, and flame speed S_L, the heat release rate per unit cross-sectional area of the Rijke tube is proportional to the flame area in this paper, $Q = \rho S_L h_R A_f/(\pi r_o^2)$. The non-dimensional fluctuating flame area A'_n is the fluctuating part of the flame area oscillation normalized by the mean flame area, $A'_n = (A_f - A_{f,0})/A_{f,0}$, and it is equal to the non-dimensional fluctuating heat release rate per unit area Q'_n.

$$A_f = \int_\Omega 2\pi r \delta(G) |\vec{\nabla} G| dr dx \tag{14}$$

2.4. Velocity Oscillation Advection

The flame is perturbed due to the acoustic velocity oscillation upstream of the flame. The input velocity oscillation at the base of the flame, $u'_{n,b}$, comes from the state-space acoustics model and is advected downstream in the level-set, as described in Eq. (15).

$$\frac{\partial u'_n}{\partial t} + u_{adv}\frac{\partial u'_n}{\partial x} = 0,\ u'_{n,b} = u'_n(x = b, t) \tag{15}$$

where u_{adv} is the advection speed of the velocity perturbation and K is the advection speed relative to the bulk velocity, $K = u_0/u_{adv} = 1.25$ in this paper. The velocity disturbance that advects along the flame is modeling a vortical disturbance, as would be excited by the incoming acoustic velocity perturbation [52]. For simplicity, we assume that the vortical velocity disturbance has the same amplitude as the acoustic velocity disturbance, to be consistent with the FDFs of Preetham et al. [47] and as nonlinearity in the flame behavior is present at this condition. A previous study by Kashinath et al. [39] explored the impact of disturbance convection speed and amplitude further. Following work by Preetham et al. [47], we only consider axial velocity perturbations throughout the domain (referred to in Ref. [47] as Velocity Model A). This makes it possible to compare the results of this work to existing flame describing functions in the literature. At every point in the level-set domain, the flame location is determined by solving the level-set equation.

2.5. Numerical Scheme

The thermoacoustic model is generated by connecting the above three individual models: acoustics, flame dynamics, and velocity perturbation advection, as shown in Fig. 3.

The flame dynamics are simulated using the level-set solver LSGEN3D [59]. To match the non-dimensional coordinate settings in LSGEN3D, we apply the following normalized variables: $x_n = x/L_f$, $r_n = r/R_f$, $y_n = y/R_f$, $z_n = z/R_f$, $u_n = u/u_0$, $t_n = tu_0/L_f$. To save computational cost, we simulate the dynamics

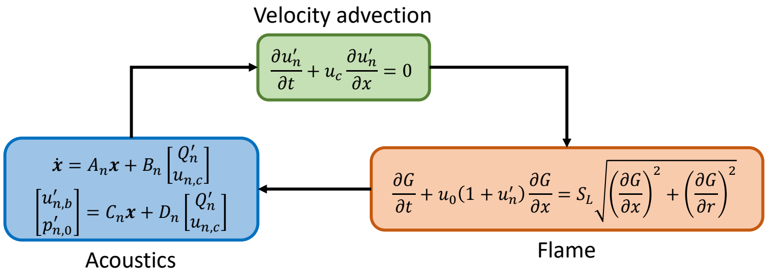

FIGURE 3. Thermoacoustic model - connecting acoustics, velocity advection, and flame models

of a two-dimensional flame in the x and r coordinates, which is a slice of an axisymmetric wedge flame along the ~~y~~third-coordinate, and the flame area is integrated assuming all dynamics are axisymmetric. Since LSGEN3D solver is designed for three-dimensional domains, we assign a small non-zero thickness in the third-coordinate. This simplification is reasonable since we only consider the fluctuating velocities in axial direction. In the numerical computation, the original G-equation in Eq. (13) is updated for axial velocity perturbation only, as in Eq. (16), where u_n' is the axial velocity oscillation component at each location in the field.

$$\frac{\partial G}{\partial t_n} + (1 + u_n') \frac{\partial G}{\partial x_n} = \frac{1}{\sqrt{1+\beta^2}} \sqrt{\left(\frac{\partial G}{\partial x_n}\right)^2 + \beta^2 \left(\frac{\partial G}{\partial r_n}\right)^2} \tag{16}$$

The domain is uniformly discretized in the ~~x, y, and z~~all the three directions. After the grid convergence test, the spatial and temporal resolution of the level-set update scheme are $\Delta x_n = 5 \times 10^{-3}$ and $\Delta t_n = 5 \times 10^{-4}$, respectively. The numbers of grid points distributed in the three coordinates are 305, 11, and 209, which means that the size of the domain is $1.52 \times 0.05 \times 1.04$. This domain captures half a branch of the wedge flame to save computational cost based on the axisymmetric assumption. The non-dimensional radius and length of the steady flame are both set to be 1.0. The width of the center-body is assumed to be zero in the simulation. To ensure flame attachment, the value of G at mesh points adjacent to the flame attachment point are held constant throughout the computation.

Based on the original level-set solver LSGEN3D, we add the acoustic models and velocity perturbation advection equation as two additional modules. The acoustics are represented by a two-input-two-output eighth-order state space model, and solved using a fixed-step fourth-order Runge-Kutta scheme. The time step size is half of the time step of the level-set solver G to ensure numerical stability considering the largest mode frequency in the system based on the stability region of the numerical scheme.

The output of the state-space model includes the velocity perturbation just upstream of the flame, at $x = b_f$ (see Eq. 15). For the velocity advection equation, we choose the same second-order upwind scheme that is used for the level-set advection, which is a back and forth error compensation and correction (BFECC) scheme [60]. The normalized advection speed is $u_{n,adv} = 0.8$ when $K = 1.25$. The time step is kept the same as that for the level-set G update, while discretizing Eq. 15 on a mesh with $\Delta x_n = 0.08$ to minimize numerical dissipation.

2.6. LQG Control Design

The LQG control design is based on a linear thermoacoustic model, which is developed from the connection between the linear acoustics state space model and a linearized FDF. The original FDF is taken from Preetham et al. [23] and shown in Fig. 4; this FDF was calculated using the same wedge-flame level-set formulation described in Sec. 2.3. Figure 4 shows the FDF for three input velocity oscillation amplitudes ϵ (where ϵ is the amplitude u_a normalized by the mean flow velocity amplitude, $\epsilon = u_a/u_0$) as well as the curve-fit applied for this study. The relative normalized velocity amplitude ϵ/ϵ_f is obtained by dividing ϵ by the normalized critical velocity fluctuation that causes flame flashback, $\epsilon_f = 1 - 1/\sqrt{1+\beta^2}$.

The curve fitting is based on a model identification method to identify the coefficients in the form of a second-order low-pass filter multiplied by a time delay term. The frequency response of the FDF amplitude suggests the existence of a zero with an increase of slope by 20 dB/decade of the frequency around

31.4 rad/sec (5 Hz), and the existence of two poles with a decrease of the slope by 20 dB/decade near 62.8 rad/sec (10 Hz) and 125.7 rad/sec (20 Hz). The phase of the FDF varies linearly with the frequency, indicating a constant delay transfer function. So the model that approximates the FDF for three velocity amplitudes contains the form in Eq. (17). The curve fit extrapolates the original data points in frequency ranges beyond 439.8 rad/sec (70 Hz). We validate the frequency response of curve-fitted FDF by harmonic acoustic forcing with higher frequencies using our simulation and the fit is accurate up to a frequency of 6283.2 rad/sec (1 kHz), which covers all the dominant acoustic modes in the system. The fit and validation are further discussed in the supplemental material. The parameters in the fitted FDF are summarized in Table. 1.

$$FTF(s) = \frac{p_1 p_2 (s + z_1) e^{-\tau s}}{z_1 (s + p_1)(s + p_2)} \tag{17}$$

Table 1. Parameters for fitted FTF at three velocity amplitudes

ϵ/ϵ_f	0.2	0.6	0.99
z_1, (rad/sec)	37.70	34.56	37.70
p_1, (rad/sec)	125.66	94.25	75.40
p_2, (rad/sec)	138.23	94.25	81.68
τ, (sec)	0.039	0.039	0.039

To formulate the linear thermoacoustic model for LQG control design, we select the FDF results at one velocity fluctuation amplitude. By connecting the fitted FDF to the linear finite-dimensional acoustic model, the linear thermoacoustic model contains the time delay term from the FDF, which makes the thermoacoustic model infinite dimensional. The literature shows that the instability frequency is near the acoustic mode frequency [15, 61]. Applying a multi-point Padé approximation [62] near the first four acoustic mode frequencies with a moment matching order of two, we reduce the order of the linear

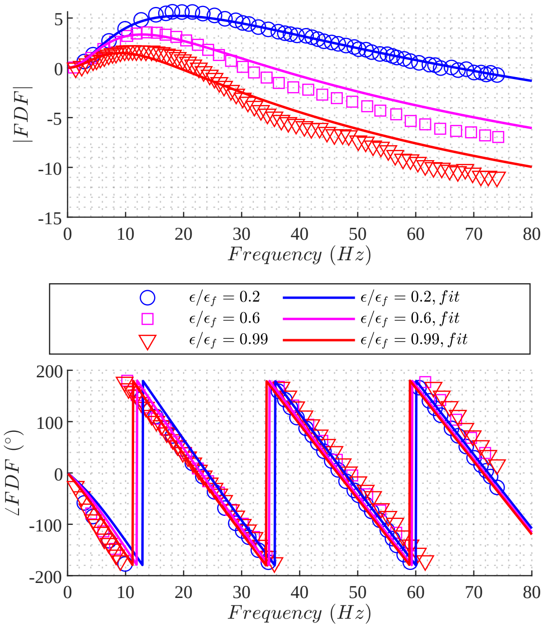

FIGURE 4. FDF - original data points and fitted curve

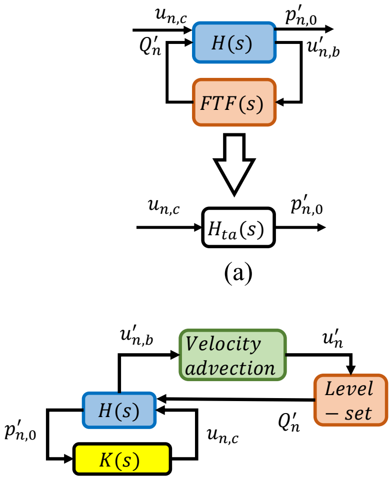

(a)

(b)

FIGURE 5. Block diagram of linear thermoacoustic model, (a) before LQG controller design, (b) controller included in the nonlinear thermoacoustic model

thermoacoustic model to eight. In the linear finite-dimensional thermoacoustic model $H_{ta}(s)$, the input is the acoustic velocity at Rijke tube inlet $u'_{n,c}$ and output is the pressure measured at the Rijke tube inlet $p'_{n,0}$, as illustrated in Fig. 5(a). Based on this single-input-single-output linear system, we design the LQG controller to suppress the output pressure oscillations. In Sec. 3.3, we explore the performance of the LQG controller for the $\epsilon/\epsilon_f = 0.2$ vs. $\epsilon/\epsilon_f = 0.99$ transfer functions.

The specific purpose of the LQG control in this work is to suppress the pressure oscillation amplitude based on the measurement of the pressure at the Rijke tube inlet. As a result, we define the quadratic cost function J to be a sum of squares of weighted pressure output $p'_{n,0}$ and weighted control input $u'_{n,c}$, as shown in Eq. (18). In the cost function, the weighting matrices Q_1 and R_1 determine the trade-off between input effort and output pressure oscillation.

Based on the generic definition form of the quadratic cost function in the idea of LQR design, we achieve the form of the weighting matrix Q_{xu}. This matrix specifies the trade-off between input and state variables, as in Eq. (19). The scalar Q_1 in the upper left diagonal represents the weight for the state variables and C is the output matrix in the linearized thermoacoustic model. The scalar R_1 in the right bottom diagonal represents the weight for the control input effort. To ensure the fast decay of the LQR regulator, the weights Q_1 and R_1 are selected to be 1×10^4 and 1, respectively.

$$\begin{aligned} J &= \frac{1}{t_{sim}} \int_0^{t_{sim}} \left({p'_{n,0}}^T Q_1 p'_{n,0} + {u'_{n,c}}^T R_1 u'_{n,c} \right) dt \\ &= \frac{1}{t_{sim}} \int_0^{t_{sim}} \left[\boldsymbol{x}^T, {u'_{n,c}}^T \right] Q_{xu} \begin{bmatrix} \boldsymbol{x} \\ u'_{n,c} \end{bmatrix} dt \end{aligned} \tag{18}$$

$$Q_{xu} = \begin{bmatrix} C^T Q_1 C & \mathbf{0} \\ \mathbf{0} & R_1 \end{bmatrix} \tag{19}$$

The design of the Kalman filter needs to specify two weighting matrices Q_2 and R_2 representing two noise sources: process noise $\boldsymbol{w}$ and measurement noise $\boldsymbol{v}$. The process noise vector $\boldsymbol{w}$ has a dimension of 8, the order of the linearized thermoacoustic model. The measurement noise $\boldsymbol{v}$ has a length of 1, the same size as the output. The covariance matrix Q_{wv} is formed in Eq. (20). Similar to the authors' earlier work [58], the intensity of Gaussian white noise sources w is assumed to be the same as that of the measurement noise v, 7×10^{-5}. This measurement noise intensity is the uncertainty level of the normalized pressure measurement. To make the state estimation error decay at a desired rate, we select the weights Q_2 and R_2 to be 1×10^5 and 1, respectively. The much larger weight on process noise makes the state estimation error decay more aggressively, which is the goal of an observer. With these weighting matrix settings in the designs of LQR and Kalman filter, the time constants corresponding to the decay rate of both the output suppression and state estimation error reduction are around 10 ms.

$$Q_{wv} = \begin{bmatrix} \boldsymbol{w} Q_2 \boldsymbol{w}^T & \mathbf{0} \\ \mathbf{0} & \boldsymbol{v} R_2 \boldsymbol{v}^T \end{bmatrix} \tag{20}$$

Based on the determined weights Q_1, R_1, Q_2, and R_2, we derive an LQG controller that has the same order as the original open-loop plant model $T(s)$. The controller $K(s)$ outputs the actuation $u'_{n,c}$ with the input from pressure signal $p'_{n,0}$. We couple the LQG controller directly in the level-set solver to control the nonlinear instability in the same way we coupled the acoustic model $H(s)$ to the level-set solver. The numerical scheme for the LQG controller is also the same as that for the acoustic model. The structure of the nonlinear thermoacoustic model with LQG controller applied is in Fig. 5(b).

3. Results

3.1. Flame Dynamics

One of the key motivations for using the wedge flame level-set formulation for this study is to capture the nonlinearity of unstable premixed flame dynamics. In particular, processes like cusping and flame-wall interaction lead to large, sudden flame area destruction and act as a saturation mechanism in the flame response [63]. Table 2 shows the parameters for the baseline case that highlights the nonlinearity of the flame dynamics and resulting thermoacoustic oscillations.

The time-domain simulation of the closed-loop thermoacoustic system, which is composed by connecting the linear acoustic model to the nonlinear flame dynamics described by the level-set solver, captures the nonlinearities in the system. The simulation is initiated with zero oscillations in pressure, velocity, and heat release within the entire level-set domain. The flame is stabilized at the center-body with a mean aspect ratio β. Initially, the normalized flame area A'_n as well as the the normalized flame heat release rate oscillation Q'_n become nonzero due to the numerical truncation error in calculating the flame area. As one of the two inputs to the acoustic model, the heat release oscillation

TABLE 2. Parameter specification of wedge flame baseline case

Parameter	**Value**
Rijke tube length, L	$0.875\ m$
Inner tube radius, r_i	$0.010\ m$
Outer tube radius, r_o	$0.046\ m$
Flame location, b_f	$0.262\ m$
Equivalence ratio, ϕ	0.8
Atmospheric pressure, p_{atm}	$1.013 \times 10^5\ Pa$
Incoming air flow velocity, u_{bulk}	$0.654\ m/sec$
Incoming mixture flow velocity, u_0	$0.586\ m/sec$
Temperature upstream of the flame, T_1	$300\ K$
Temperature rise across the flame, ΔT	$100\ K$
Mean heat release rate per unit area, Q_0	$8.657 \times 10^4\ W/m^2$
Flame aspect ratio, β	2
Flame speed, S_L	$0.262\ m/sec$
Convection parameter, K	1.25
Ratio of specific heats, γ	1.4

Q'_n leads to a nonzero velocity output upstream of the flame $u'_{n,b}$, which is convected downstream and perturbs the flame. If the system operates at an unstable condition, this coupling excites an exponential growth of the pressure oscillation in the thermoacoustic system. After the exponential growth, the normalized pressure at the Rijke tube inlet $p'_{n,0}$ and flame area A'_n both arrive at a limit cycle due to the saturation of the flame area. The time series of the two variables in the baseline case are shown in Fig. 6. The instability amplitude of the limit cycle pressure oscillation is around $2.2 \times 10^{-3} p_{atm}$ (or 223 Pa). As the flame area fluctuations become large, the mean flame area appears to increase, such that the mean of the A'_n signal is approximately 0.2. This is a known

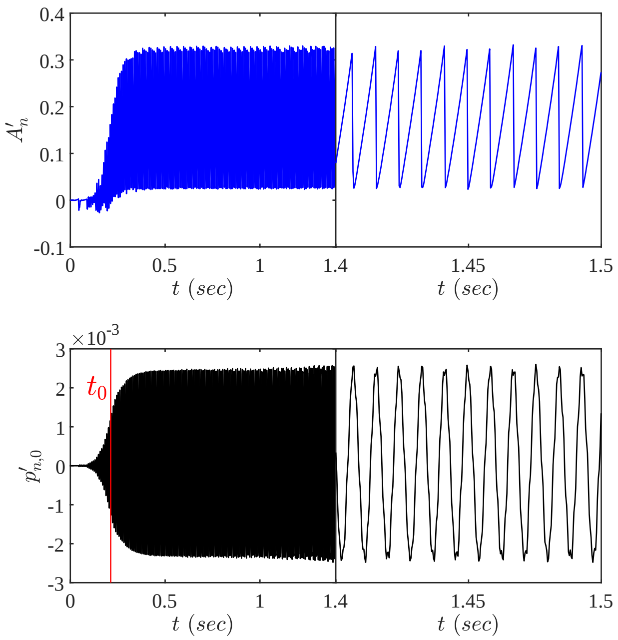

FIGURE 6. Time series of the normalized flame area and the normalized pressure at Rijke tube inlet in a limit cycle onset

issue with the level-set formulation and arises from the fact that energy is not conserved and discussion of this issue can be found in Preetham [64].

Computing the fast Fourier transform (FFT) of the signal during the limit cycle oscillations, we obtain the spectra of the two signals shown in Fig. 7. The pressure spectrum has a dominant oscillation at a frequency around 728.8 rad/sec (116 Hz), which is close to the first acoustic mode in the Rijke tube, 716.3 rad/sec (114 Hz). Due to the nonlinearity in the flame dynamics, the flame area spectrum contains multiple frequencies that are harmonics of the fundamental mode.

The shape evolution of the center-body attached wedge flame over one half period of the limit cycle oscillation is illustrated in Fig. 8. Two mechanisms of flame area fluctuation saturation are visible in these images (and indicated by arrows): flame cusping and flame/wall interaction. Flame cusping appears periodically as a result of the propagation of the curved flame normal to itself [65], as shown by the arrow in the plot at phase 0°. Between the phase angles of

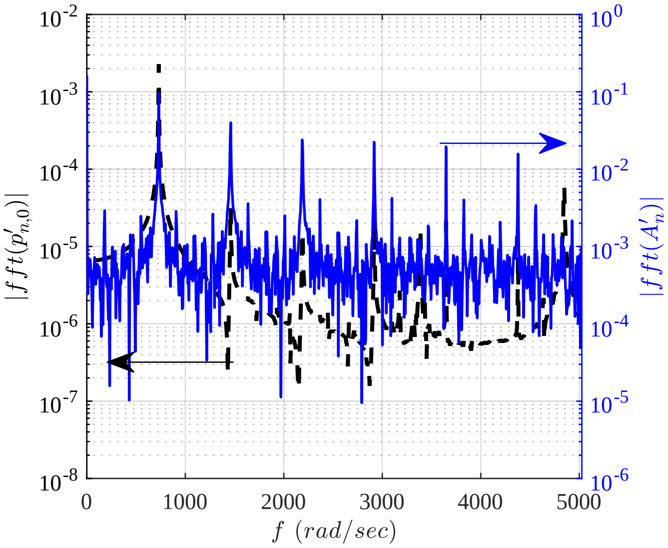

FIGURE 7. Spectra of the normalized flame area and the normalized pressure at Rijke tube inlet at limit cycle duration

90° and 135°, the flame tip impinges on the wall, which leads to a rapid drop in flame area. These effects are why the flame area oscillation is cyclic but not harmonic in Fig. 6.

3.2. Stability Mapping

Based on the time-domain simulation, we investigate the system stability over two parameters: flame location and temperature rise across the flame. There are a number of different oscillatory states the system can take [15], including periodic oscillation with one frequency, periodic oscillation with multiple frequencies, quasi-periodic oscillation, and chaotic oscillation. We initially mapped the stability of the system over a wide range of parameters: $b/L = 0.1 - 0.9$ and $\Delta T = 100 - 300$ K, then selected smaller ranges with interesting dynamical behaviors over which we performed a finer stability mapping. The final mapping includes flame locations between $b_f/L = 0.1$ and $b_f/L = 0.4$ with an interval of 0.025 b_f/L at a temperature rise $\Delta T = 100$ K across the flame. The temperature rise ΔT varies between $\Delta T = 100$ K and

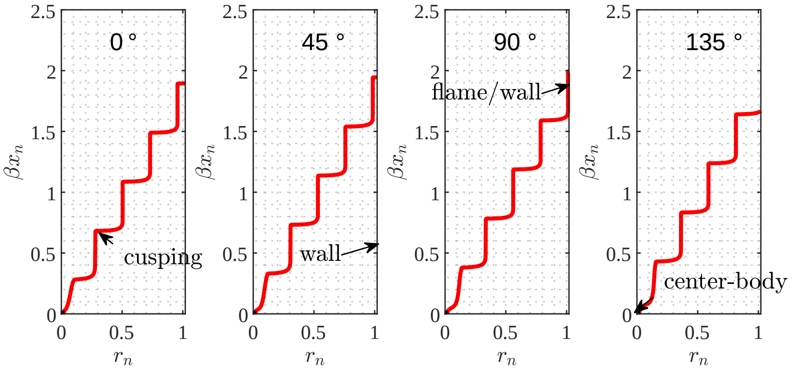

FIGURE 8. Wedge flame evolution within a half cycle in the baseline case: $b_f/L = 0.3$, $\Delta T = 100K$

$\Delta T = 300$ K with a 20 K interval of at a flame location $b_f/L = 0.3$. With the same parameter space, we also analyze the sensitivity of the LQG controller's performance to different thermoacoustic oscillation characteristics in Sec. 3.3.

3.2.1. Sensitivity to flame location

Figure 9 shows the normalized pressure oscillation in time domain for four of the 13 operating conditions between $b_f/L = 0.1 - 0.4$; the complete set of results is shown in the supplementary material. As the flame location varies in the Rijke tube, the instability characteristics in the system vary as well. For all the cases here, the system initially oscillates at the frequency of the first mode and, in some cases, other frequencies appear at later times. This is consistent with the fact that the first modes' eigenvalues have the largest positive real parts among all the cases. The detailed distribution of the linearized thermoacoustic system's eigenvalues is shown in Fig. 10. The linearized system consists of linear acoustic model and linearized FDF extracted at the input velocity amplitude $\epsilon/\epsilon_f = 0.99$.

The instability amplitude increases until the flame area oscillation saturates. In the early oscillations, multiple unstable modes exist for cases with flame

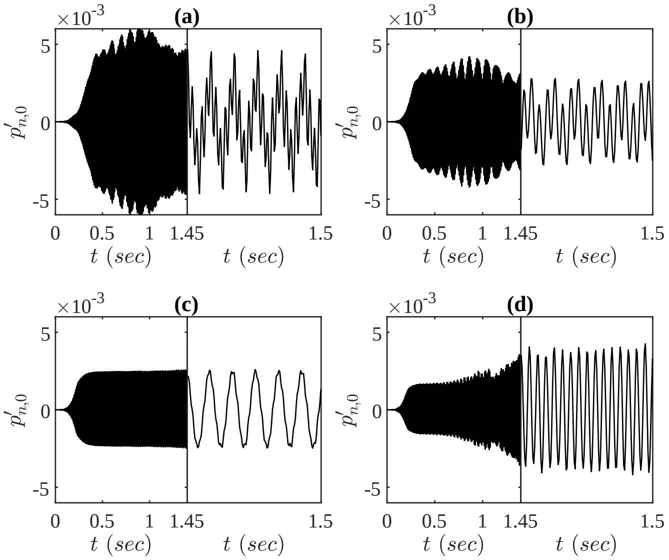

FIGURE 9. Time series of the normalized pressure oscillation at four different flame locations: (a) $b_f/L = 0.1$, (b) $b_f/L = 0.2$, (c) $b_f/L = 0.3$, (d) $b_f/L = 0.4$, $\Delta T = 100$ K

located at $b_f/L = 0.1$ and $b_f/L = 0.2$ when multiple modes have growth rates at similar orders of magnitude. If the saturated oscillation in velocity just upstream of the flame does not exceed the critical amplitude that causes flame flashback ϵ_f, the saturation amplitude is constant, as in cases $b_f/L = 0.15$ and $b_f/L = 0.325$ in the supplementary material. When the oscillation amplitude of the velocity at flame base exceeds the critical amplitude ϵ_f, flame flashback should happen, in theory. However, in the level-set solver, flame attachment at the center-body is enforced and it prevents flame flashback from happening in simulation. In this situation, the flame area oscillation amplitude will remain constant yet continues to act as the input to the undamped acoustic system. When one of the multiple harmonics in the flame area oscillation input is close to an acoustic mode frequency in the marginally stable acoustic model, the oscillation amplitude of that mode will increase linearly with respect to time, as observed in case $b_f/L = 0.4$. This is also observed in more cases when temperature rise across the flame varies, as shown in Fig. 12.

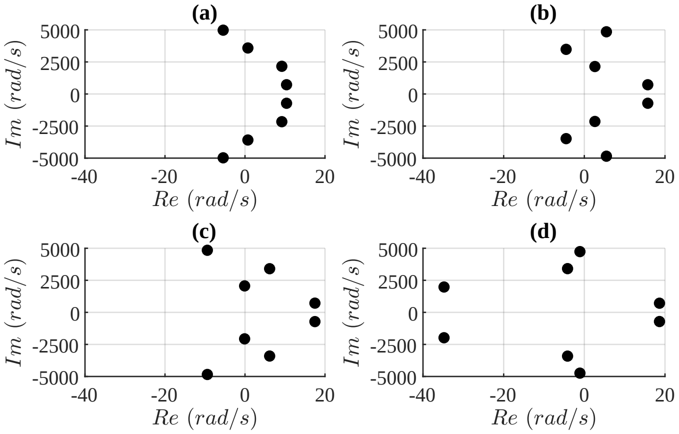

FIGURE 10. Eigenvalue distribution for the linearized thermoacoustic system at four flame locations with the flame transfer function at the velocity excitation amplitude of $\epsilon/\epsilon_f = 0.99$: (a) $b_f/L = 0.1$, (b) $b_f/L = 0.2$, (c) $b_f/L = 0.3$, (d) $b_f/L = 0.4$, $\Delta T = 100$ K

The four plots shown in Fig. 9 illustrate examples of different instability progressions through time. In Fig. 9(a) with $b_f/L = 0.1$, the system transitions from the first mode of oscillation to the third mode between $t = 1.45$ sec and $t = 1.50$ sec. At a flame location of $b_f/L = 0.2$ in Fig. 9(b), the system behaves similarly to that in Fig. 9(a), except now the shift is to the second mode. For the baseline case in Fig. 9(c), the system only oscillates at the first mode. Finally, for a flame location of $b_f/L = 0.4$, the system shifts from the first mode to the second mode entirely at an earlier time than the other cases. Which mode the system transitions to depends on the growth rate of the new dominant mode at the transition. Additionally, the location of the flame relative to the shape of each mode is indicative of which modes will be excited. For example, in the $b_f/L = 0.2$ case, the flame is located at the third mode's pressure node and hence, this mode can not be excited. For the baseline case $b_f/L = 0.3$, the node of the second mode is close to the flame location and this mode does not appear. The mode shapes for the first four acoustic modes are included in the supplementary material for all the cases studied, including 13 flame locations and 11 temperature rises cases.

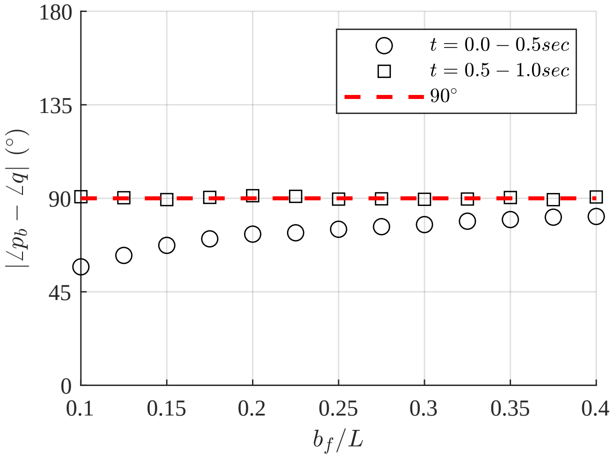

FIGURE 11. Phase difference between oscillations of mode 1 pressure at flame location and flame area in two durations for different flame locations, $\Delta T = 100$ K

The location of the flame relative to the spatial mode shape, especially the pressure node, explains why some modes are not excited. While alignment of the flame and a pressure anti-node is conducive for thermoacoustic coupling, the pressure and heat release rate oscillations must also be aligned in time. In the modeled system dynamics, no acoustic energy losses exist and the net acoustic energy input is purely the driving effect, quantified by the Rayleigh index. This term is the integral of the product between pressure and heat release oscillations over space and time. Since the flame is acoustically compact at flame location b_f, the Rayleigh index is simplified to a time domain integral. The key parameter that affects the Rayleigh index is the phase difference between the oscillations of pressure at the flame location and the flame heat release rate. The phase difference is summarized in Fig. 11, for the cases with different flame locations.

Figure 11 shows the phase difference, determined using the FFT of the two signals, in the first 0.5 seconds. Among all the different flame location cases, the phase difference of the first mode is smaller than 90° in the first 0.5 seconds, which means a positive driving of the mode. As the flame is located further down the tube, the phase difference becomes closer to 90° and the driving effect becomes weaker; this agrees with the initial exponential increase of the pressure oscillation amplitude observed in the time series results for the four cases in Fig. 9 and all the cases in the supplementary material. After the first 0.5 seconds, the phase difference of the first mode is close to 90° for all the cases regardless of flame location; this lack of thermoacoustic driving causes the saturated pressure oscillation behavior in the time series data between 0.5 and 1.0 seconds.

3.2.2. Sensitivity to temperature rise across the flame

Variations in the instability characteristics also occur when the temperature rise across the flame changes. The temperature rise varies from 100 K to 300 K with an interval of 20 K, while the flame location is kept the same as that in the baseline case $b_f/L = 0.3$. The temperature rise is varied by changing the air flow velocity in the outer tube without changing any parameters of the flame. In all cases, the low-Mach assumption is still valid. Similar with the analysis of sensitivity to the flame location in Sec. 3.2.1, we include the pressure time series, frequency spectra, and acoustic mode shapes for all the temperature rise cases in the supplementary material for reference.

Figure 12 shows the normalized pressure oscillations in the time domain for four of the 11 cases. The $\Delta T = 200$ K and $\Delta T = 220$ K temperature rise cases correspond to a linear growth state oscillating at the first mode around 628.3 rad/sec (100 Hz) early in the simulation. At this condition, the flame area fluctuation has saturated before 0.5 sec. as a result of kinematic restoration and flame/wall interaction. Therefore, the bidirectional coupling between flame heat release dynamics and acoustic dynamics effectively becomes uni-directional. As a result, the flame (which now has a constant, saturated amplitude) drives the acoustics at a resonant frequency, with a constant (i.e., saturated) amplitude excitation. It is a property of linear resonant dynamic systems that driving them with a constant-amplitude excitation at resonance results in a linear response growth with time, as opposed to exponential growth with time.

The other two cases oscillate at a limit cycle amplitude for multiple modes. Based on the spectra for the pressure signal in the supplementary material, the

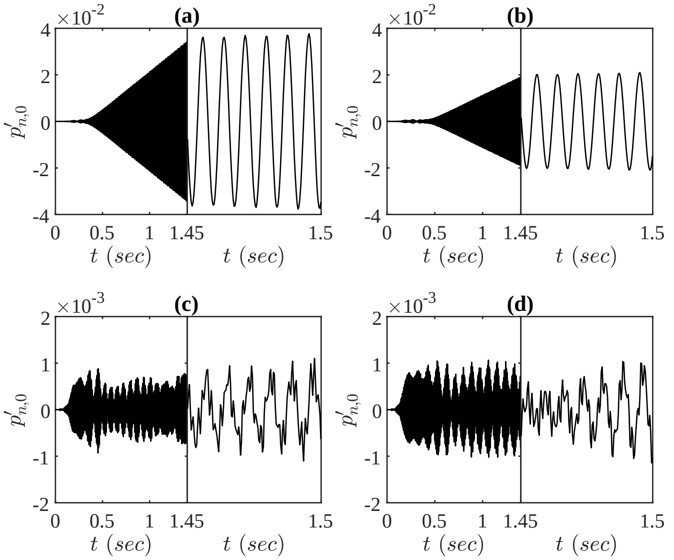

FIGURE 12. Time series of the normalized pressure oscillation at four different temperature rises: (a) $\Delta T = 200$ K, (b) $\Delta T = 220$ K, (c) $\Delta T = 240$ K, (d) $\Delta T = 260$ K, $b_f/L = 0.3$

dominant modes for case $\Delta T = 240$ K are the first, third, and the fourth modes. The dominant modes for case $\Delta T = 260$ K are all the first four modes. The eigenvalue distribution for the linearized thermoacoustic system composed of linear acoustics and FDF at $\epsilon/\epsilon_f = 0.99$ is displayed in Fig. 13. The eigenvalue shows the first mode has the largest growth rate for all the cases, which is consistent with the initially excited first mode oscillations in all the cases.

Similar to the analysis for variations in flame location, we apply both spatial and temporal phase difference analysis for the sensitivity to temperature rise. For all the cases, the flame is located near the pressure node for the second mode. As a result, the second mode is much weaker in amplitude compared to the other three modes in these cases. We further examine the phase difference between the pressure at the flame location and the heat release rate to explain why the mode is excited. The time-averaged phase differences for two time durations are summarized in Fig. 14 for the first mode. The phase difference moves away from 90° initially and towards 90° later when the temperature rise across the flame

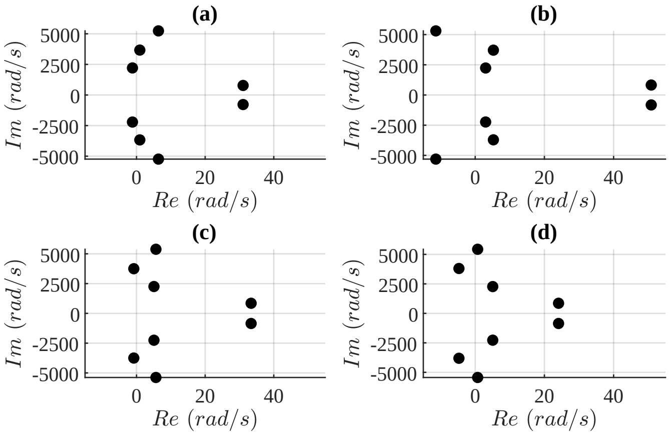

FIGURE 13. Eigenvalue distribution for the linearized thermoacoustic system at four different temperature rises across the flame with the flame transfer function at the velocity excitation amplitude of $\epsilon/\epsilon_f = 0.99$: (a) $\Delta T = 200$ K, (b) $\Delta T = 220$ K, (c) $\Delta T = 240$ K, (d) $\Delta T = 260$ K, $b_f/L = 0.3$

increases from 100 K to 220 K. The phase difference stays around 90° when the temperature rise is between 240 K and 300 K, which explains the relatively small amplitude of the pressure oscillations in the early simulation for those cases with higher temperature rises. From $0.5 - 1.0$ sec, the phase difference is near 90° when the temperature rise is smaller than 140 K and greater than 240 K, and smaller than 90° when temperature rise is between 140 and 240 K. This agrees with the pressure oscillation in time domain in Fig. 12 for four cases with different temperature rises.

Compared to the flame location variation studies, the stability behavior changes more dramatically with temperature rise variations. The larger dependence of the system stability on temperature rise is related to the larger variations of phase difference between the pressure and heat release rate oscillations. The phase difference depends on two physical processes: (1) acoustic propagation in the regions upstream and downstream of the flame considering wave reflections; (2) phase delay from velocity to heat release in the flame transfer function. The change of flame location b_f affects both the length b_f

and $(L - b_f)$ and the first mode frequency $f_{a,1}$ of the acoustic propagation. The change of temperature rise ΔT across the flame affects both the speed of sound in the region downstream of the flame c_2 and the first mode frequency $f_{a,1}$. These changes lead to phase changes corresponding to the acoustic wave propagation times in both regions upstream and downstream of the flame, as described in Eq. (21). Additionally, the first mode frequency change causes the phase difference change between velocity and heat release, as seen in the frequency response of the FDF phase in Fig. 4. The dependence of the phase difference between velocity at the flame base and heat release on frequency is approximately linear with the FDF time delay τ_{FDF} representing the slope, as described in Eq. (22).

$$\psi_1 = \frac{2b_f}{c_1} \cdot f_{a,1}(b_f, \Delta T),\ \psi_2 = \frac{2(L - b_f)}{c_2(\Delta T)} \cdot f_{a,1}(b_f, \Delta T) \tag{21}$$

$$\psi_{FDF} = \tau_{FDF} \cdot f_{a,1}(b_f, \Delta T), \tau_{FDF} \approx 0.039sec \tag{22}$$

The examples that show the variation of the phase difference caused by the changes in flame location and temperature rise are summarized in Table 3 and Table 4, respectively.

The variations in the three phase values ψ_1, ψ_2, and ψ_{FDF} are at similar order of magnitude to the variation of the phase difference between pressure at flame location and heat release, shown in Fig. 11. Similar conclusions exist for the cases with temperature rise changes. The detailed phase difference summary is in the supplementary material for later times during the simulation.

3.3. Controller Performance

The control designed with the method described in Sec. 2.6 is applied to the thermoacoustic model in all the cases discussed in the previous sections. For cases with different flame locations or temperature rises, a different LQG controller is designed with the same weights $Q_1 = 1 \times 10^4$, $R_1 = 1$, $Q_2 = 1 \times 10^5$, and $R_2 = 1$. The following three non-dimensional metrics are used to

TABLE 3. Examples of showing the phase variations caused by changes in flame location, $\Delta T = 100K$

Variable	**Case A**	**Case B**	**Variation B-A**
b_f/L	0.3	0.325	0.025
$f_{a,1},\ (rad/sec)$	714.4	713.1	-1.3
$c_1,\ (m/sec)$	347.2	347.2	0
$c_2,\ (m/sec)$	400.9	400.9	0
$\psi_1,\ (^\circ)$	70.7	76.5	5.8
$\psi_2,\ (^\circ)$	117.4	112.1	-5.3
$\psi_{FDF},\ (^\circ)$	1596.3	1593.5	2.8
$\lvert\angle p_b - \angle q\rvert,\ (^\circ)$	77.4	79.0	1.6

evaluate the LQG control performance: (1) root mean square (RMS) of all the state variables $J_{x,1}$, which quantifies the variability of the system before control activation; (2) RMS of all the state variables after the control activation $J_{x,2}$, which quantifies the variability of the system after control activation; and (3) RMS of the control input $J_{u,2}$. The definitions of the three LQG performance metrics are shown in Eqs. (23) and (24). The variables t_1 and t_2 represent the duration of time before and after LQG control activation.

$$J_{x,1} = \sqrt{\frac{1}{t_1}\int_0^{t_1} \left({p'_{n,0}}^T Q_1 p'_{n,0}\right) dt},\ J_{x,2} = \sqrt{\frac{1}{t_2}\int_{t_1}^{t_1+t_2} \left({p'_{n,0}}^T Q_1 p'_{n,0}\right) dt} \tag{23}$$

$$J_{u,2} = \sqrt{\frac{1}{t_2}\int_{t_1}^{t_1+t_2} \left({u'_{n,c}}^T R_1 u'_{n,c}\right) dt} \tag{24}$$

The baseline control activation time for this study is defined as $2t_0$, which is approximately the onset of the instability limit cycle in the baseline case ($b_f/L = 0.3, \Delta T = 300$ K). The time t_0 is defined following Culler et al. [66] as the mid-point of the instability growth in the pressure signal and is called

TABLE 4. Examples of showing the phase variations caused by changes in temperature rise, $b_f/L = 0.3$

Variable	**Case A**	**Case B**	**Variation B-A**
$\Delta T,\ (K)$	100	120	20
$f_{a,1},\ (rad/sec)$	688.0	699.3	11.3
$c_1,\ (m/sec)$	347.2	347.2	0
$c_2,\ (m/sec)$	400.9	410.8	0.9
$\psi_1,\ (^\circ)$	59.0	58.5	-0.5
$\psi_2,\ (^\circ)$	113.1	112.2	-0.9
$\psi_{FDF},\ (^\circ)$	1537.4	1562.7	25.3
$\lvert\angle p_b - \angle q\rvert,\ (^\circ)$	77.4	61.6	-15.8

"halfway moment" of the transition, as shown in Fig. 6. The moment of the LQG control activation for all cases is the same ($t_{LQG} = 0.426$ sec) as in the baseline for comparison purposes.

3.3.1. Sensitivity to choice of flame transfer function

In the LQG control design, different FTFs can be selected as linearizations for the FDF to obtain a linearized thermoacoustic system. The different FTFs correspond to different oscillation amplitudes of the incoming velocity upstream of the flame. The higher the velocity amplitude is, the more nonlinear the flame dynamics are. To study the performance of the linear control on the thermoacoustic oscillations considering nonlinear flame dynamics, we compare the performance of two LQG controllers that are designed using FDFs with velocity oscillation amplitude at $\epsilon/\epsilon_f = 0.2$ and $\epsilon/\epsilon_f = 0.99$.

Figure 15 shows four variables in time domain in the controlled baseline system, including the flame area, control input, pressure at the Rijke tube inlet, and the velocity just upstream of the flame. Both controllers are applied at $t = 2t_0$. Based on the behaviors of the pressure oscillations after the control

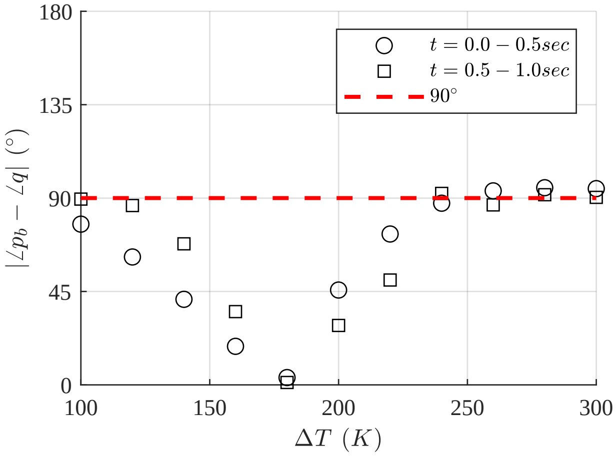

FIGURE 14. Phase difference between oscillations of mode 1 pressure at flame location and flame area in two durations for different temperature rises, $b_f/L = 0.3$

activation, both controllers suppress the originally large amplitude oscillation by at least 70%. This shows that the linear control performs well in attenuating the nonlinear thermoacoustic oscillations. The difference only lies in the oscillation amplitude of the closed-loop controlled system. The system controlled by the LQG controller designed using $\text{FDF}_{\epsilon/\epsilon_f=0.99}$ arrives at a stable state with a much smaller pressure amplitude. This means that the LQG controller designed from the FDF at a higher velocity amplitude performs better, at least in the continuing suppression of the instability.

The Bode plots of the two LQG controllers designed using two FDFs are compared in Fig. 16. The LQG controller from FDF at a larger amplitude $\epsilon/\epsilon_f = 0.99$ does a better job in suppressing the instability even with a lower gain at the first mode frequency 728.8 rad/sec (116 Hz). The gain of the LQG controller designed from the FDF at the smaller amplitude $\epsilon/\epsilon_f = 0.2$ has a larger amplitude (100.7) than that (76.2) of the LQG controller from FDF at a larger amplitude $\epsilon/\epsilon_f = 0.99$ at the first mode frequency. The key parameter that affects the performance of an LQG controller in this case is the phase delay the controller adds to the control signal with measurement of the pressure at

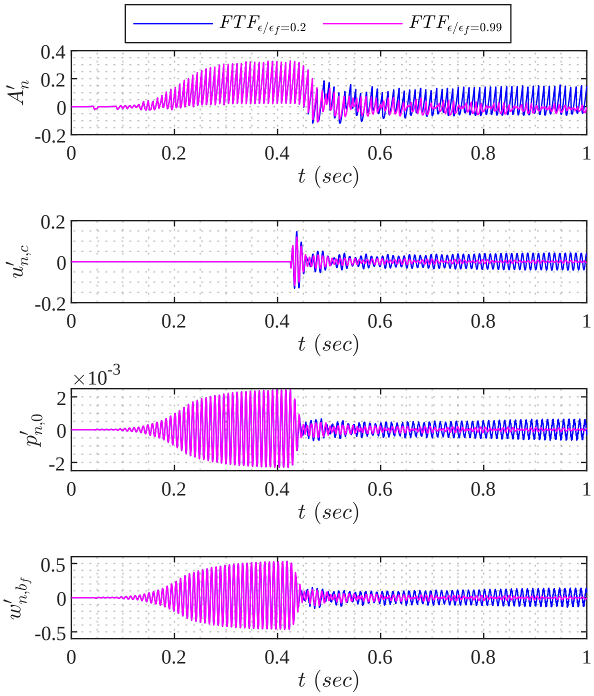

FIGURE 15. Time series of the normalized flame area, control input, normalized pressure at the Rijke tube inlet, and normalized velocity right upstream of flame in the baseline case: $b_f/L = 0.3$, Δ T=100 K, $t_{LQG} = 2t_0$=0.426 sec, two FTF applied in the LQG control design

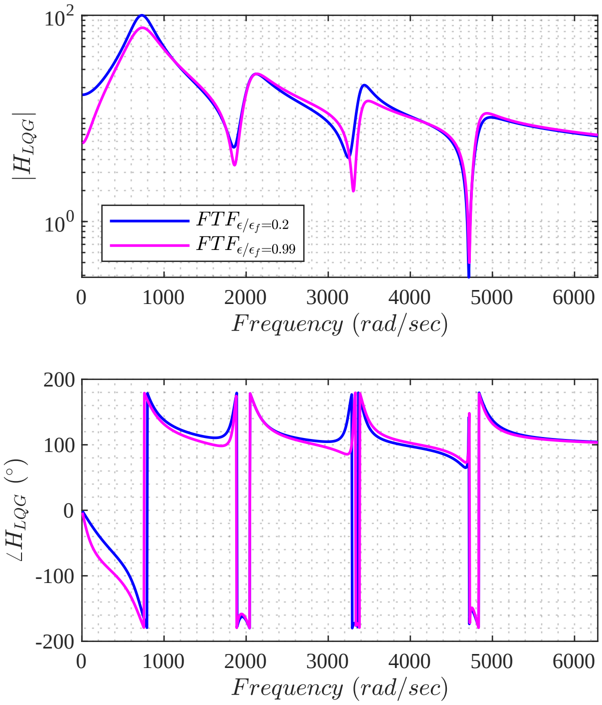

Figure 16. Bode plots of the LQG controllers using two FTFs at incoming velocity oscillation amplitudes of $\epsilon/\epsilon_f = 0.2$ and $\epsilon/\epsilon_f = 0.99$

Rijke tube inlet. The output velocity of the LQG controller corresponding to the FDF at $\epsilon/\epsilon_f = 0.99$ is further delayed by a phase of about 18° than the velocity from the LQG corresponding to the smaller amplitude $\epsilon/\epsilon_f = 0.2$. As shown by "Case A" in Table 3, the open-loop phase difference between the pressure at flame location and heat release is 77.4°, which causes driving of the thermoacoustic system and growth of the oscillation amplitude. These phase differences in the control input signal velocity at Rijke tube inlet cause a phase shift in the velocity at the flame base, making the phase difference between pressure at the flame and heat release rate 161.1°, which is greater than 90°, resulting in thermoacoustic damping and suppression of the oscillation.

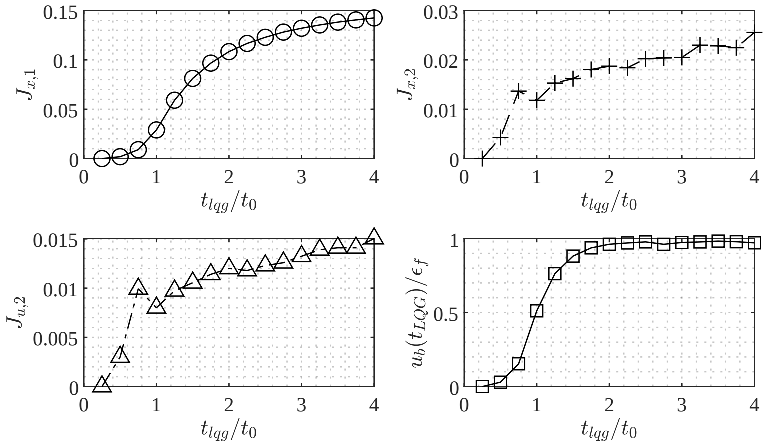

FIGURE 17. Dependence of LQG controller's performance on LQG activation moment

3.3.2. Sensitivity to controller activation moment

In this section, we study the performance of the same LQG controller activated at different times during the instability for the baseline case. This study highlights the degree to which the moment when the LQG control is activated matters in determining the performance of the LQG controller. For consistency, we use the controller designed for the higher amplitude oscillation $\epsilon/\epsilon_f = 0.99$ throughout the remainder of this article since this controller works better in the earlier application on the baseline at $t_{LQG} = 2t_0$. The results for the baseline case, $b_f/L = 0.3,\ \Delta T = 100$ K, are shown in Fig. 17. The results indicate that earlier activation of the controller reduces the control effort needed to attenuate the instability. This is mostly due to the fact that the system experiencing the instability onset process contains higher RMS of the system variability if averaged over a longer duration starting from the initial moment of the simulation. As a result, for most activation moments, the LQG control effort scales with the system oscillation energy before the LQG control activation. The bottom right plot shows the flame base velocity at the moment just before the LQG activation and it represents the instability amplitude of the system for reference.

3.3.3. Sensitivity to flame location

For all the different flame locations from $b_f/L = 0.1$ to $b_f/L = 0.4$, we design the LQG control based on the linearized thermoacoustic system combining the linear acoustic model and the FDF at $\epsilon/\epsilon_f = 0.99$. All the LQG controllers are activated at the same moment $t_{LQG} = 2t_0 = 0.426$ sec, so as to compare to the baseline case. Figure 18 shows the dependence of the LQG controller performance on flame location. The pressure oscillation before and after the control, denoted by the performance metrics $J_{x,1}$ and $J_{x,2}$, respectively, indicate that the linear LQG controller helps to reduce the pressure oscillation amplitude by almost one order of magnitude for most cases. The open-loop system's pressure oscillation decreases nearly monotonically with respect to the increasing flame location closer to Rijke tube exit, which can be explained by the open-loop phase difference between the pressure at the flame location and the flame heat release in Fig. 11.

The controlled closed-loop pressure oscillation decreases at first but later increases with an increasing flame location. For flame location between $b_f/L = 0.1$ and $b_f/L = 0.325$, the dependence of the control input effort and the controlled output behave similarly with the system variability before the activation of LQG control, as seen in the top left plot in Fig. 18. When the flame location is larger than $b_f/L = 0.325$, the RMS values of the control input effort and the controlled output increase with increasing flame location, which is different from dependence of RMS output on flame location before LQG activation.

3.3.4. Sensitivity to temperature rise

Similarly, we examine the performance of the LQG controller for different temperature rises. The original system without any control varies dramatically with temperature rise, as shown in Fig. 12. This behavior can be explained based on the phase difference between the pressure at the flame location and the heat release for different temperature rise cases in Fig. 14.

At the time instant when control is applied, the pressure oscillation and the velocity oscillation initially increase and later decrease rapidly with increased

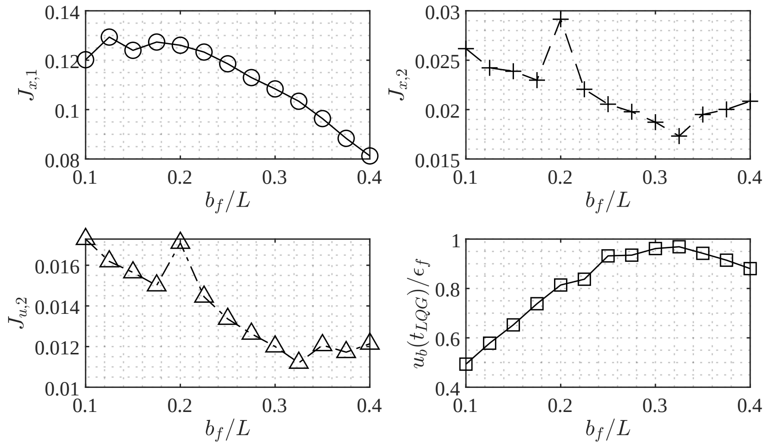

FIGURE 18. Dependence of LQG controller's performance on flame location

temperature rise until 200 K. When the temperature rise increases above 220 K, the oscillation amplitude increases, as shown in Fig. 19. Both the root mean squared controlled output and control input behave similarly with the root mean squared output before the LQG control activation for temperature rises in the range between 100 K and 200 K. When the temperature rise exceeds 200 K, the control input effort is more governed by the amplitude of the flame base velocity. If the amplitude is closer to ϵ_f in the case with temperature rise of $\Delta T = 220$ K and 300 K, the control input is smaller than the cases when the velocity amplitude is further away from ϵ_f. The controlled oscillation achieves nearly an order of magnitude reduction in cases when the temperature rise is smaller than 200 K and the velocity amplitude upstream of the flame exceeds ϵ_f. When the velocity oscillation amplitude at flame base is smaller than ϵ_f, the controller performs worse in attenuating the oscillation amplitude.

4. Conclusions

This article furthers the study of linear control in suppressing the thermoacoustic oscillations including nonlinear flame dynamics in a one dimensional combustor. This study develops a framework that can co-simulate the linear

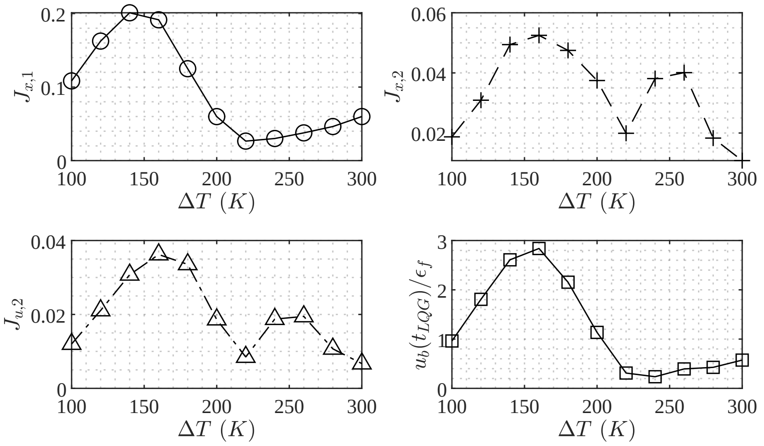

FIGURE 19. Dependence of LQG controller's performance on temperature rise in the acoustic model

acoustics, nonlinear flame dynamics, and linear control in the time domain. The framework is a modified version of the level-set solver that is initially used to simulate the nonlinear heat release response of flames to incoming flow velocity perturbations. Based on the time-domain simulation for thermoacoustic systems both with and without control applied, this article systematically analyzes the dependence of instability behavior and control performance on varied flame locations and temperature rises across the flame.

Specifically, the article makes the following conclusions in the modeling and control of thermoacoustic oscillation considering nonlinear flame dynamics.

1. In the time domain simulation of the system connecting linear acoustics and level-set solver described flame dynamics, the nonlinear flame behaviors are captured in a baseline case with a limit cycle instability. Multiple harmonics exist in the flame area oscillation and they are caused by the formed nonlinear flame cusping and flame-wall interaction.
2. The instability characteristics, including oscillation frequency components and amplitude, vary both with changes in flame location and temperature rise. The change of temperature rise by 20 K leads to a more dramatic

change in stability behaviors compared with the change of flame location by $0.025L$. The spatial acoustic mode analysis shows that the mode whose node overlaps with flame location will not be excited. The temporal phase analysis explains when the mode is excited, which is driven by the phase difference between the oscillations of pressure at the flame location and heat release. When the magnitude of the phase difference is smaller than 90°, the positive driving effect excites the mode. The phase difference change among the cases with different flame locations or temperature rises is governed by two processes: acoustic propagation time variation and phase delay variation in the flame transfer function.

3. The linear control designed based on the linear thermoacoustic system that includes a flame describing function at one incoming velocity oscillation amplitude works to suppress the thermoacoustic oscillation with nonlinear flame dynamics. Comparing the two different LQG controllers, the LQG control designed considering the FDF with higher input velocity oscillation amplitude $\epsilon = 0.99\epsilon_f$ achieves a lower controlled oscillation amplitude than the LQG control designed with a lower amplitude $\epsilon = 0.2\epsilon_f$.
4. Analyzing the variation of the LQG control performance with respect to the control activation moment, flame location, and temperature rise finds that the control performance is mostly determined by the oscillation energy in the original open-loop system before the LQG control application. For some cases, the correlation between the control effort and the open-loop system oscillation amplitude is not strictly positive, which can be caused by the discrepancy between the system used for LQG design with a higher velocity amplitude and the system to be controlled with a lower velocity amplitude.

5. Acknowledgements

This work was supported by the National Science Foundation under Grant No. CMMI-1728307. Any opinions, findings, and conclusions or recommendations expressed in this material are those of the authors and do not necessarily reflect the views of the National Science Foundation.

References

[1] T. C. Lieuwen, V. Yang, Combustion instabilities in gas turbine engines: operational experience, fundamental mechanisms, and modeling, American Institute of Aeronautics and Astronautics, 2005.

[2] J. W. S. B. Rayleigh, The theory of sound, Vol. 2, Macmillan, 1896.

[3] N. Noiray, D. Durox, T. Schuller, S. Candel, A unified framework for nonlinear combustion instability analysis based on the flame describing function, J. Fluid Mech. 615 (2008) 139.

[4] P. Palies, D. Durox, T. Schuller, S. Candel, Nonlinear combustion instability analysis based on the flame describing function applied to turbulent premixed swirling flames, Combust. Flame 158 (10) (2011) 1980–1991.

[5] X. Han, J. Li, A. S. Morgans, Prediction of combustion instability limit cycle oscillations by combining flame describing function simulations with a thermoacoustic network model, Combust. Flame 162 (10) (2015) 3632–3647.

[6] S. Candel, Combustion dynamics and control: progress and challenges, Proc. Combust. Inst. 29 (1) (2002) 1–28.

[7] A. P. Dowling, A. S. Morgans, Feedback control of combustion oscillations, Annu. Rev. Fluid Mech. 37 (2005) 151–182.

[8] L. Crocco, S.-I. Cheng, Theory of combustion instability in liquid propellant rocket motors, Tech. rep., Princeton University NJ (1956).

[9] W. Lang, T. Poinsot, S. Candel, Active control of combustion instability, Combust. Flame 70 (3) (1987) 281–289.

[10] D. Zhao, Transient growth of flow disturbances in triggering a rijke tube combustion instability, Combust. Flame 159 (6) (2012) 2126–2137.

[11] T. Lieuwen, Y. Neumeier, Nonlinear pressure-heat release transfer function measurements in a premixed combustor, Proc. Combust. Inst. 29 (1) (2002) 99–105.

[12] D. Kim, J. G. Lee, B. D. Quay, D. A. Santavicca, K. Kim, S. Srinivasan, Effect of flame structure on the flame transfer function in a premixed gas turbine combustor, J. Eng. Gas Turb. Power 132 (2) (2010).

[13] Y. Xia, D. Laera, W. P. Jones, A. S. Morgans, Numerical prediction of the flame describing function and thermoacoustic limit cycle for a pressurised gas turbine combustor, Combust. Sci. Technol. 191 (5-6) (2019) 979–1002.

[14] M. Haeringer, M. Merk, W. Polifke, Inclusion of higher harmonics in the flame describing function for predicting limit cycles of self-excited combustion instabilities, Proc. Combust. Inst. 37 (4) (2019) 5255–5262.

[15] K. Kashinath, I. C. Waugh, M. P. Juniper, Nonlinear self-excited thermoacoustic oscillations of a ducted premixed flame: bifurcations and routes to chaos, J. Fluid Mech. 761 (2014) 399–430.

[16] I. C. Waugh, K. Kashinath, M. P. Juniper, Matrix-free continuation of limit cycles and their bifurcations for a ducted premixed flame, J. Fluid Mech. 759 (2014) 1–27.

[17] A. Orchini, S. Illingworth, M. Juniper, Frequency domain and time domain analysis of thermoacoustic oscillations with wave-based acoustics, J. Fluid Mech. 775 (2015) 387.

[18] D. Laera, T. Schuller, K. Prieur, D. Durox, S. M. Camporeale, S. Candel, Flame describing function analysis of spinning and standing modes in an annular combustor and comparison with experiments, Combust. Flame 184 (2017) 136–152.

[19] M. Matalon, B. J. Matkowsky, Flames as gasdynamic discontinuities, J. Fluid Mech. 124 (1982) 239–259.

[20] F. Baillot, D. Durox, R. Prud'Homme, Experimental and theoretical study of a premixed vibrating flame, Combust. Flame 88 (1992) pp–149.

[21] M. Fleifil, A. M. Annaswamy, Z. Ghoneim, A. F. Ghoniem, Response of a laminar premixed flame to flow oscillations: A kinematic model and thermoacoustic instability results, Combust. Flame 106 (4) (1996) 487–510.

[22] S. Ducruix, D. Durox, S. Candel, Theoretical and experimental determinations of the transfer function of a laminar premixed flame, Proc. Combust. Inst. 28 (2000) 765–773.

[23] Preetham, T. Lieuwen, Nonlinear flame-flow transfer function calculations: flow disturbance celerity effects, in: 40th AIAA/ASME/SAE/ASEE Joint Propulsion Conference and Exhibit, 2004, p. 4035.

[24] S. Hemchandra, N. Peters, T. Lieuwen, Heat release response of acoustically forced turbulent premixed flames—role of kinematic restoration, Proc. Combust. Inst. 33 (1) (2011) 1609–1617.

[25] A. Dowling, A kinematic model of a ducted flame, J. Fluid Mech. 394 (1) (1999) 51–72.

[26] K. Kashinath, S. Hemchandra, M. P. Juniper, Nonlinear phenomena in thermoacoustic systems with premixed flames, J. Eng. Gas Turb. Power 135 (2013) 061502–1.

[27] B. Schuermans, V. Bellucci, C. O. Paschereit, Thermoacoustic modeling and control of multi burner combustion systems, in: Turbo Expo: Power for Land, Sea, and Air, Vol. 36851, 2003, pp. 509–519.

[28] Y.-C. Chu, A. P. Dowling, K. Glover, Robust control of combustion oscillations, in: Proceedings of the 1998 IEEE International Conference on Control Applications, Vol. 2, IEEE, 1998, pp. 1165–1169.

[29] Y.-C. Chu, K. Glover, A. P. Dowling, Control of combustion oscillations via h_∞ loop-shaping, μ-analysis and integral quadratic constraints, Automatica 39 (2) (2003) 219–231.

[30] D. Zhao, X. Li, Minimizing transient energy growth of nonlinear thermoacoustic oscillations, Int. J. Heat Mass Tran. 81 (2015) 188–197.

[31] J. Hathout, A. Annaswamy, M. Fleifil, A. Ghoniem, A model-based active control design for thermoacoustic instability, Combust. Sci. Technol. 132 (1-6) (1998) 99–138.

[32] D. Campos-Delgado, K. Zhou, D. Allgood, S. Acharya, Active control of combustion instabilities using model-based controllers, Combust. Sci. Technol. 175 (1) (2003) 27–53.

[33] J. R. Hervas, D. Zhao, M. Reyhanoglu, Observer-based control of rijke-type combustion instability, in: AIP Conference Proceedings, Vol. 1637, American Institute of Physics, 2014, pp. 899–906.

[34] R. E. Kalman, A new approach to linear filtering and prediction problems, J. Basic Eng-T ASME (1960).

[35] B. D. Anderson, J. B. Moore, Optimal control: linear quadratic methods, Courier Corporation, 2007.

[36] M. Fleifil, J. Hathout, A. Annaswamy, A. Ghoniem, The origin of secondary peaks with active control of thermoacoustic instability, Combust. Sci. Technol. 133 (4-6) (1998) 227–265.

[37] A. M. Annaswamy, M. Fleifil, J. W. Rumsey, R. Prasanth, J.-P. Hathout, A. F. Ghoniem, Thermoacoustic instability: model-based optimal control designs and experimental validation, IEEE T. Contr. Syst. T. 8 (6) (2000) 905–918.

[38] S. Murugappan, S. Acharya, D. Allgood, S. Park, A. Annaswamy, A. Ghoniem, Optimal control of a swirl-stabilized spray combustor using

system identification approach, Combust. Sci. Technol. 175 (1) (2003) 55–81.

[39] K. Kashinath, S. Hemchandra, M. P. Juniper, Nonlinear thermoacoustics of ducted premixed flames: the influence of perturbation convection speed, Combust. Flame 160 (12) (2013) 2856–2865.

[40] L. Kabiraj, R. Sujith, P. Wahi, Bifurcations of self-excited ducted laminar premixed flames, J. Eng. Gas Turb. Power 134 (3) (2012).

[41] L. Kabiraj, R. Sujith, Nonlinear self-excited thermoacoustic oscillations: intermittency and flame blowout, J. Fluid Mech. 713 (376-397) (2012) 13.

[42] J. Li, A. S. Morgans, Time domain simulations of nonlinear thermoacoustic behaviour in a simple combustor using a wave-based approach, J. Sound Vib. 346 (2015) 345–360.

[43] T. Schuller, D. Durox, S. Candel, A unified model for the prediction of laminar flame transfer functions: comparisons between conical and v-flame dynamics, Combust. Flame 134 (1-2) (2003) 21–34.

[44] T. Lieuwen, Nonlinear kinematic response of premixed flames to harmonic velocity disturbances, Proc. Combust. Inst. 30 (2) (2005) 1725–1732.

[45] D. Durox, T. Schuller, N. Noiray, S. Candel, Experimental analysis of nonlinear flame transfer functions for different flame geometries, Proc. Combust. Inst. 32 (1) (2009) 1391–1398.

[46] R. S. Blumenthal, P. Subramanian, R. Sujith, W. Polifke, Novel perspectives on the dynamics of premixed flames, Combust. Flame 160 (7) (2013) 1215–1224.

[47] Preetham, H. Santosh, T. Lieuwen, Dynamics of laminar premixed flames forced by harmonic velocity disturbances, J. Propul. Power 24 (6) (2008) 1390–1402.

[48] T. Steinbacher, A. Albayrak, A. Ghani, W. Polifke, Consequences of flame geometry for the acoustic response of premixed flames, Combust. Flame 199 (2019) 411–428.

[49] S. Candel, D. Durox, T. Schuller, P. Palies, J.-F. Bourgouin, J. P. Moeck, Progress and challenges in swirling flame dynamics, C.R. Mecanique 340 (11-12) (2012) 758–768.

[50] K. T. Kim, J. G. Lee, H. J. Lee, B. D. Quay, D. A. Santavicca, Characterization of forced flame response of swirl-stabilized turbulent lean-premixed flames in a gas turbine combustor, J. Eng. Gas Turb. Power 132 (4) (2010).

[51] D. Durox, J. P. Moeck, J.-F. Bourgouin, P. Morenton, M. Viallon, T. Schuller, S. Candel, Flame dynamics of a variable swirl number system and instability control, Combust. Flame 160 (9) (2013) 1729–1742.

[52] B. D. Bellows, M. K. Bobba, A. Forte, J. M. Seitzman, T. Lieuwen, Flame transfer function saturation mechanisms in a swirl-stabilized combustor, Proc. Combust. Inst. 31 (2) (2007) 3181–3188.

[53] S. K. Thumuluru, T. Lieuwen, Characterization of acoustically forced swirl flame dynamics, Proc. Combust. Inst. 32 (2) (2009) 2893–2900.

[54] X. Chen, J. O'Connor, H. Fathy, Optimizing thermoacoustic characterization experiments for identifiability improves both parameter estimation accuracy and closed-loop controller robustness guarantees, Combust. Sci. Technol. (2021) 1–26.

[55] A. Dowling, S. Stow, Acoustic analysis of gas turbine combustors, J. Propul. Power 19 (2003) 751–764.

[56] A. P. Dowling, Nonlinear self-excited oscillations of a ducted flame, J. Fluid Mech. 346 (1997) 271–290.

[57] S. Hemchandra, Premixed flame response to equivalence ratio fluctuations: Comparison between reduced order modeling and detailed computations, Combust. Flame 159 (12) (2012) 3530–3543.

[58] X. Chen, H. Fathy, J. O'Connor, Impact of sensor placement on mode observability and lqg control of a thermoacoustic system, in: International Federation of Automatic Control, 2020, pp. 4214–4221.

[59] S. Hemchandra, Dynamics of turbulent premixed flames in acoustic fields, Ph.D. thesis, Georgia Institute of Technology (2009).

[60] T. F. Dupont, Y. Liu, Back and forth error compensation and correction methods for removing errors induced by uneven gradients of the level set function, J Comput. Phys. 190 (1) (2003) 311–324.

[61] J. Li, A. S. Morgans, Feedback control of combustion instabilities from within limit cycle oscillations using h_∞ loop-shaping and the ν-gap metric, P. Roy. Soc. A-Math. Phy. 472 (2191) (2016) 20150821.

[62] M. Celik, O. Ocali, M. A. Tan, A. Atalar, Pole-zero computation in microwave circuits using multipoint padé approximation, IEEE T. Circuits-I 42 (1) (1995) 6–13.

[63] R. Balachandran, B. Ayoola, C. Kaminski, A. Dowling, E. Mastorakos, Experimental investigation of the nonlinear response of turbulent premixed flames to imposed inlet velocity oscillations, Combust. Flame 143 (1-2) (2005) 37–55.

[64] Preetham, Modeling the response of premixed flames to flow disturbances, Ph.D. thesis, Georgia Institute of Technology (2007).

[65] D.-H. Shin, T. Lieuwen, Flame wrinkle destruction processes in harmonically forced, laminar premixed flames, Combust. Flame 159 (11) (2012) 3312–3322.

[66] W. Culler, X. Chen, J. Samarasinghe, S. Peluso, D. Santavicca, J. O'Connor, The effect of variable fuel staging transients on self-excited instabilities in a multiple-nozzle combustor, Combust. Flame 194 (2018) 472–484.